IOPscience iopscience.iop.org

Home Search Collections Journals About Contact us My IOPscience

Velocimetry of edge turbulence during the dithering L–H transition with dynamic programming based time-delay estimation technique in the EAST superconducting tokamak

This content has been downloaded from IOPscience. Please scroll down to see the full text.

2013 Plasma Phys. Control. Fusion 55 105006

(http://iopscience.iop.org/0741-3335/55/10/105006)

View the table of contents for this issue, or go to the journal homepage for more

Download details:

IP Address: 202.127.206.25
This content was downloaded on 20/06/2014 at 01:10

Please note that terms and conditions apply.

Plasma Phys. Control. Fusion **55** (2013) 105006 (11pp) doi:10.1088/0741-3335/55/10/105006

Velocimetry of edge turbulence during the dithering L–H transition with dynamic programming based time-delay estimation technique in the EAST superconducting tokamak

L M Shao[1], G S Xu[1], S C Liu[1], S J Zweben[2], B N Wan[1], H Y Guo[1,3], A D Liu[4], R Chen[1], B Cao[1], W Zhang[1], H Q Wang[1], L Wang[1], S Y Ding[1], N Yan[1], G H Hu[1], H Xiong[1], L Chen[1], Y L Liu[1], N Zhao[1] and Y L Li[1]

[1] Institute of Plasma Physics, Chinese Academy of Sciences, Hefei 230031, People's Republic of China
[2] Princeton Plasma Physics Laboratory, PO Box 451, Princeton, NJ 08540, USA
[3] Tri Alpha Energy, Inc., PO Box 7010, Rancho Santa Margarita, CA 92688, USA
[4] CAS Key Laboratory of Plasma Physics, Department of Modern Physics, University of Science and Technology of China, Hefei 230026, People's Republic of China

E-mail: shaolm@ipp.ac.cn

Received 23 April 2013, in final form 30 July 2013
Published 2 September 2013
Online at stacks.iop.org/PPCF/55/105006

Abstract
A dual gas puff imaging (GPI) system has been successfully assembled on the Experimental Advanced Superconducting Tokamak (EAST) and applied for the study of the dithering L–H transition in the 2012 spring campaign. A new method i.e., the dynamic programming based time-delay estimation technique, has been applied to the 64 × 64 pixels GPI video images to yield time-dependent two-dimensional velocity fields at the plasma edge on EAST. Local poloidal flow velocities up to $\sim -3\,\mathrm{km\,s^{-1}}$ (in the electron diamagnetic direction) and radial flow velocities up to $\sim -2\,\mathrm{km\,s^{-1}}$ (inward) are found inside the separatrix during a dithering burst. The radial and poloidal cross-correlation length, flow velocity and auto-correlation time inside the separatrix increase preceding the dithering burst and decrease following the dithering burst. These observations provide strong evidence for the shear flows playing an important role during the dithering L–H transition.

(Some figures may appear in colour only in the online journal)

1. Introduction

The edge plasma turbulence in magnetically confined devices is widely considered to play an important role in driving heat and particle anomalous transport in tokamak [1] and other toroidal magnetically confined devices [2]. The edge turbulence is also considered to play an important role in the L–H transition physics [3]. The recent advance in the two-dimensional (2D) visualization of turbulent structures has greatly enhanced the understanding of the underlying dynamics. Several 2D diagnostics have been developed for visualization of the turbulent structures, including beam emission spectroscopy (BES) [4, 5], electron cyclotron emission imaging (ECEI) [6, 7], microwave imaging reflectometry (MIR) [8, 9], and gas puff imaging (GPI) [10, 11]. ECEI takes advantage of focusing optics and frequency selection based on the gradient in the strength of the toroidal magnetic field to form a 2D image (in the poloidal plane) of electron temperature. MIR makes use of similar microwave frequencies and collection optics to image the plasma cut-off layer, enabling localized and precise measurements of density fluctuation. BES and GPI diagnostics are based on the detection of line emission from neutrals in the edge plasma.

 © 2013 IOP Publishing Ltd Printed in the UK & the USA

A 2D (poloidal versus radial) edge plasma GPI diagnostic has been assembled successfully on the Experimental Advanced Superconducting Tokamak (EAST) before its 2012 spring campaign. Previously, two reciprocating probe systems have been used in EAST to study the edge turbulence. However, the application of the probe inside the separatrix is prohibited by high heat load on the probe in high heating power discharges. Taking advantage of its 2D visualization capability and the high spatial–temporal resolution, the GPI diagnostic has been used to investigate several important issues, such as turbulence [12], blobs [13], zonal flow [14], L–H transition [14, 15] and edge localized modes (ELMs) [16, 17] in NSTX and Alcator C-Mod. GPI introduces a neutral gas puff into the edge plasma to image the turbulence motion. To minimize the perturbation of the edge plasma by the GPI gas puffing, low-Z gases, such as He and D_2, are used. The visible line emission (He I line at 587.6 nm or Dα line at 656.3 nm) from a puffed gas cloud near the last closed flux surface (LCFS) is imaged with a fast framing camera. These measurements are performed with spatial resolution for one pixel of 2 mm and time resolution of 2.56 μs, which are much smaller than the typically size ($\sim$20 mm) and auto-correlation time ($\sim$10 μs) of the edge plasma turbulent structures in EAST.

The derivation of the radial and poloidal flow pattern in the plasma edge can contribute significantly to the understanding of turbulence and its relationship to edge transport. The time-delay estimation (TDE) method is conventionally used to calculate the turbulence velocity fields based on the cross-correlation of fluctuation signals at two spatially separated (within a fluctuation correlation length) locations. For a given channel separation, a time-dependent velocity can thus be determined. Specific TDE methods have been developed in several magnetic devices by different groups to characterize turbulence behavior, including time-delay cross-correlation methods [18, 19], the wavelet-based method [20], and the dynamic programing technique [21, 22]. The time-resolved cross-correlation method is based on finding the time delay of the maximum of the cross-correlation function of two signals within a short-time-window. The wavelet-based TDE methods are used in some case to take advantage of higher time resolution compared to the traditional Fourier transform TDE methods. The wavelet-based TDE method has been applied to BES in DIII-D, and the 2D time-delay cross-correlation analysis is used in NSTX [15] or C-Mod [14] conventionally.

For achieving a higher frequency response and sensitivity [21, 22], dynamic programming based TDE analysis is chosen to analyze the GPI data in EAST. The dynamic programming is a recursive optimization mathematical method for solving a problem composed of overlapping sub-problems with an optimal substructure. In the present TDE technique, dynamic programming works as a vector matching algorithm to estimate a temporal shift for the best match between coherent parts of two signals. A technique of this kind has previously been applied to particle imaging velocimetry with 2D spatial data in experimental fluid dynamics [23]. In this paper, the technique is extended and applied to temporal data from GPI to obtain the fluctuations of the time-delay, i.e., the time-varying time-delay.

This paper is organized as follows. The setup of the GPI is presented in section 2. The method used to process video images from GPI and yield time-dependent velocity fields is given in section 3. The results from dynamic programming based TDE applied to GPI data during dithering L–H transitions are shown in section 4. A summary and discussion of the results is given in section 5, along with possible plans for further work.

2. Diagnostic setup

Two GPI systems have been implemented on EAST [24] before the 2012 spring campaign. The basic dual GPI diagnostic on EAST has been described in detail elsewhere [11], so only a brief description will be given here. The layout of the dual GPI diagnostic on EAST is illustrated in figure 1(*a*). Two 16 cm long gas manifolds, each having 16 pinholes covered by thin molybdenum tiles, are mounted on the inner wall behind the radio frequency (RF) limiter shadow beside the port C and E. Each manifold is oriented to produce a cloud of gas extending along the local poloidal direction near the separatrix (the boundary between open and closed field lines). The gas puff from either of these two manifolds is viewed along the edge magnetic field lines through a reentrant port (telescope) about 178 cm away. These two GPI systems separated by $\sim$66.6° toroidally and $\sim$100° poloidally (see figure 1(*b*)) are vertically symmetrical about the midplane. The gas puff is used to localize the light emission (He I line emission at 587.6 nm is detected in EAST, and the main working gas of EAST is deuterium) in order to obtain a cross-section of the turbulence in the radial versus poloidal plane. The camera image is centered on the magnetic separatrix (see figure 1(*b*)) and the sight line of telescope is about 6.4° above or below the outer midplane.

For these experiments, the images were recorded with two Phantom V710 cameras, each coupled to the vessel via a coherent fiber-optic bundle inserted into a reentrant vacuum port. The Phantom V710 camera is equipped with a custom charge coupled device (CCD) chip capable of storing 32 GB (12-bit dynamic range) image frames of 64 × 64 pixels at a rate of 391 000 frames s^{-1}. The camera has a 13 × 13 cm^2 (radial versus poloidal) viewing area perpendicular to the total magnetic field at the gas cloud. The minimal wave-number of the turbulence that GPI can measure is $k_{pol}(\min) \sim 2\pi/15\,\text{cm} \sim 0.5\,\text{cm}^{-1}$ (the length along the poloidal direction inside the separatrix in GPI's viewing region is around 15 cm in EAST), while the maximal wave-number of the turbulence that GPI can measure is $k_{pol}(\max) \sim 2\pi/0.2\,\text{cm} \sim 3\,\text{cm}^{-1}$ (the spatial resolution is 0.2 cm). Thus, the GPI mainly measures the mid-size and micro-size turbulence.

Under the collisional radiative approximation, the intensity of the line emission depends on the local electron density n_e and temperature T_e as

$$S = n_0 f\,(n_e, T_e)\,A, \tag{1}$$

where A is the radiative decay rate of the observed line, n_0 is the local neutral density, and $f\,(n_e, T_e)$ is a function providing the density ratio between neutrals in the upper and lower transition states [25]. The dependence on n_e and T_e, through

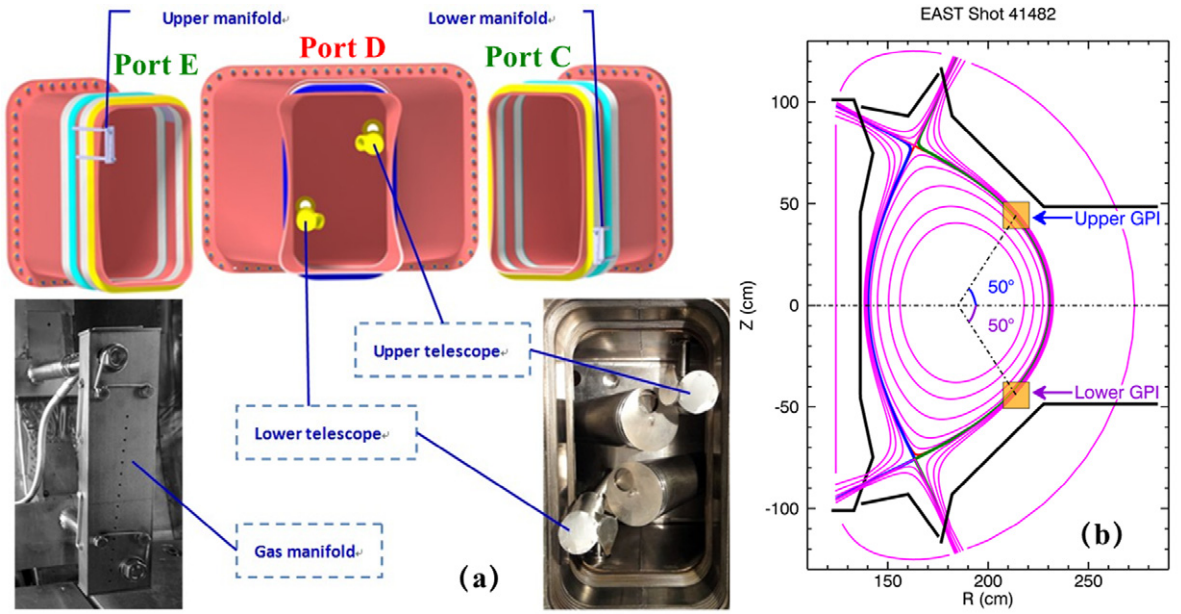

Figure 1. (*a*) Illustration of two GPI diagnostic systems on EAST. Gas manifold of upper GPI is located at top left side of port E and that of lower GPI is located at bottom right side of port C. The two telescopes are located in the center at port D. (*b*) Cross section of two GPI system poloidally separated by ∼100°.

the function f, modulates the line emission due to fluctuations in either of these two plasma parameters. The edge electron temperature and density of typical discharge in EAST is similar to that in NSTX [11], and the local emissivity of the He I near the peak of light emission on NSTX varies as $S \propto n_e^{0.7} T_e^{0.5}$ according to DEGAS 2 code [26]. Currently, it is impossible to distinguish the density fluctuations from the temperature fluctuations that GPI measures on EAST. It should be noted that the use of the GPI diagnostic is constrained by the line emission profile of the neutral gas. Namely, the brightness of any given emission line has a limited radial extent in regions of steep temperature and density gradients, since the ionization of neutral gas decreases the signal far inside of separatrix. Supersonic nozzles can be chosen to slightly increase the intensity profile inside the separatrix. In all cases, it is difficult to use the GPI diagnostic very far from the separatrix in EAST and other devices due to the low signal levels.

3. Dynamic programming based TDE analysis

The dynamic programming technique is robust to moderate changes in average time-delay amplitudes in the data, and does not require optimization of analysis parameters for small changes. The algorithm seeks to divide a large problem into incremental steps such that at any stage, an optimal solution on the sub-problem is known. It has been used to estimate the flow fluctuation velocity for BES in DIII-D [21]. Here it is utilized to estimate the time-delay between two partially correlated, one-dimensional (1D) temporal signals obtained from fluctuation measurements using GPI diagnostic.

To compute the time-delay between two partially correlated time signals (for example, $U[i]$ and $V[j]$) by the dynamic programming algorithm based TDE technique (the technique described below is exactly the same as in [21]),

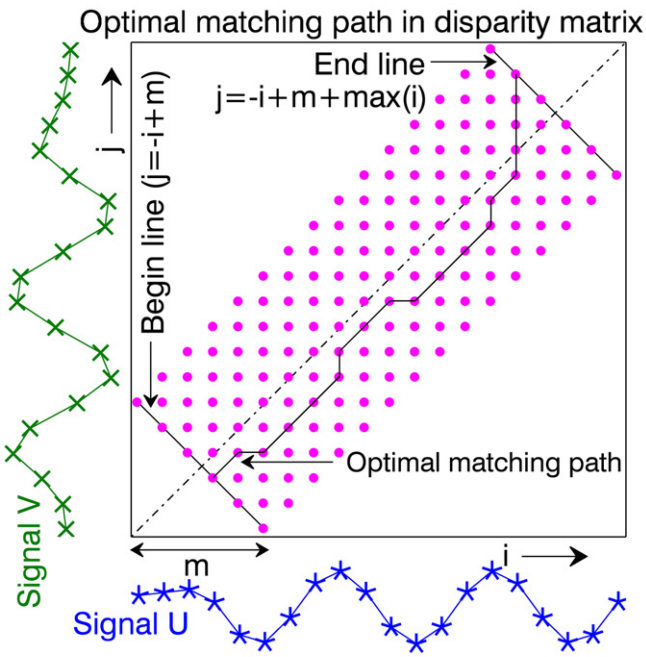

Figure 2. Illustration of local matching residual matrix of two partially correlated time signals with a probable optimal matching path.

the implementation process described below should be done step by step. First a 'local matching residual' function matrix $d[i, j]$ is calculated by finding all possible absolute shifts between the signals, i.e.,

$$d[i, j] = |U[i] - V[j]|. \tag{2}$$

The size of this matrix is proportional to the record length of the signals i.e., $\max(i)$, $\max(j)$. An illustration of the 'local matching residual' function matrix d is shown in figure 2.

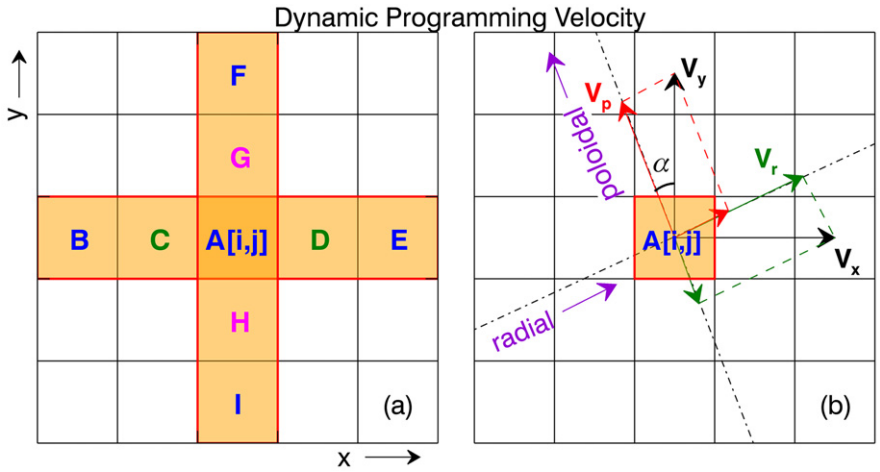

Figure 3. (*a*) Spatial arrangement of pixels around a reference pixel A for dynamic programming based on TDE. (*b*) Illustration of velocity projection method of flow velocity, α is the angle between poloidally magnetic line and vertical direction.

If there is no or a constant time-delay between signals $U[i]$ and $V[j]$, the minimal local matching residual $d[i, j]$ will lie in diagonal line or a diagonally shifted straight line of this matrix. When the displacement the diagonally shifted straight line is extracted, the time-delay between the two signals will be known. However, $U[i]$ and $V[i]$ always have a time-varying time-delay, so the minimal local matching residual will not along a straight line path. The dynamic programming algorithm offers an efficient way to find out the optimal path, which has a minimum total of the local matching residual. The sum over the optimal path of the local matching residual function is defined as the 'accumulated residual function' $D[i, j]$, which follows the recursive equation

$$D[i, j] = \min \begin{Bmatrix} D[i, j-1] + d[i, j-1] + d[i, j] & ① \\ D[i-1, j-1] + 2 & \\ \quad \times ([d[i-1, j-1] + d[i, j]) & ② \\ D[i-1, j] + d[i-1, j] + d[i, j] & ③ \end{Bmatrix}. \tag{3}$$

The initial conditions used to recursively calculate the D[i,j] function are

$$D[i, j] = \begin{Bmatrix} 0, & \text{if } i + j = m \\ \infty, & \text{if } |i - j| > m \text{ or } i + j < m \end{Bmatrix}, \tag{4}$$

where m is the maximum absolute displacement selected to search the matching paths. Sometimes, to achieve a more temporal precision and fractional time-step resolution, the above procedural steps can be iteratively repeated, even with interpolation [23].

There are many paths from the beginning line to the end line, but only the one with minimal accumulated residual function $D[i,j]$ is defined as the optimal matching path as shown in figure 2. Obviously, the last local matching residual $d[i,j]$ along the optimal line also lies in end line (see figure 2). Thus, from the beginning line ($j = -i+m$) on 'local matching residual' function matrix d to the ending line ($j = -i + m + \max(i)$), only $m+1$ optimal matching candidates (paths) can be found from all possible paths. A 'position encoding' technique is used to record locations of every local matching residual ahead $d[i,j]$ (one of $d[i-1, j]$, $d[i-1, j-1]$ and $d[i, j-1]$) lying in the $m + 1$ paths when calculating $D[i,j]$ during searching each of these paths here. By calculating recursive equation (3) for each $D[i,j]$ in each path, if the first equation is satisfied, position$[i, j] = 0$(position$[i, j]$ is the positional code of $d[i,j]$ calculated by 'position encoding' technique); if the second equation is satisfied, position $[i, j] = 1$; and position $[i, j] = 2$ if the third equation is satisfied. Then just to find the minimum value of all the last $D[i,j]$ lying in the $m + 1$ candidate paths (also lying in the end line), the optimal matching path will be achieved. To find all local matching residual $d[i,j]$ and its shift displace j–i lying in this optimal path, a decoding position $[i,j]$ technique is used here, which follows the recursive equation

$$d = \begin{Bmatrix} d[i-1, j], & \text{if position } [i, j] = 0 & ① \\ d[i-1, j-1], & \text{if position } [i, j] = 1 & ② \\ d[i, j-1], & \text{if position } [i, j] = 2 & ③ \end{Bmatrix}. \tag{5}$$

The mean of all shift displace j–i of $d[i,j]$ on this optimal path is the time-delay between the time series.

Before calculating flow velocity from fluctuating measurements of GPI by dynamic programming based on TDE, a series of preprocessing is needed. First, each frame in the raw-data sequence is filtered with a 2D median filter (using a three-point width) to remove noise spikes from the image frame. Camera images for each frame were normalized to the time-averaged image of the gas cloud to eliminate systematic pixel-to-pixel spatial variations due to the fiber bundle and optics. This can be done by simply dividing the brightness image of each frame by the time-averaged frame. For each pixel in the interesting region of a frame, a short time series is created consisting of the normalized intensities at this pixel for ± 32 frames (0 represents the present frame), i.e., for $\sim$164 μs (>7 times longer than averaged auto-correlation time of edge turbulence in EAST).

Then the dynamic programming is applied to two adjacent pixels in the video images, since a one pixel interval is most suitable for calculations as can be seen in figure 3(*a*). Velocities $v_{BA}\, v_{CD}\, v_{AE}\, v_{IA}\, v_{HG}\, v_{AF}$ are obtained in this way. So velocity of

pixel A at present frame is defined by

$$v_{Ax} = \frac{(v_{BA} + v_{CD} + v_{AE})}{3}, \tag{6}$$

$$v_{Ay} = \frac{(v_{IA} + v_{HG} + v_{AF})}{3} \tag{7}$$

To eliminate an unreal time-delay [27], the minimum time-delay is limited to 0.1 T ($T = 1/390\,804$ s, i.e. 1/frame rate) and thus the maximum velocity of local flow is up to $\sim\pm 16\,\mathrm{km\,s^{-1}}$. When the absolute value of calculated velocity is larger than $16\,\mathrm{km\,s^{-1}}$, the absolute value of a calculated time-delay is less than 0.1 T. These unrealistically large calculated velocities will be replaced by an interpolated value. This can be simply done by averaging calculated velocities of nearby pixels (using a 3×3 kernel boxcar average here). To smooth the time resolution of velocity, 75% time series, i.e. 48 frames overlapping is used for each pixel from one frame to next calculated frame when applying this method to GPI data.

As shown in figure 1(*b*), the last closed magnetic line (separatrix) is tilted in the viewing region by $\sim 31^\circ$ (slightly varying from shot to shot and time to time) from the vertical direction. To obtain velocity fields in radial and poloidal directions, the evaluated velocity fields in the horizontal and vertical directions calculated by applying the above method should be rotated by α (α is the angle between poloidally magnetic line and vertical direction. mostly, α is thought as a constant and equal to the angle between separatrix and vertical direction) in the counter-clockwise direction for each pixel of present frame (see figure 3(*b*))

$$v_r\,[i,\,j] = v_x\,[i,\,j]\cos\alpha + v_y\,[i,\,j]\sin\alpha, \tag{8}$$

$$v_p\,[i,\,j] = -v_x\,[i,\,j]\sin\alpha + v_y\,[i,\,j]\cos\alpha, \tag{9}$$

where $v_x[i,\,j]$ and $v_y[i,\,j]$ are the initially estimated velocities of each pixel in horizontal and poloidal directions at present frame, α is the angle between poloidal magnetic line and vertical direction. Then, radial and poloidal velocity arrays of a frame are rotated by α and averaged over a poloidal range (24 pixels i.e. 4.8 mm are used here) within the GPI field of view to obtain a 'zonal' average of these velocities. Actually, averaging over a poloidal range is only an approximation to the $m = 0$ poloidal structure of this flow, it is the best that can be done to evaluate the shear flow with the limited poloidal range of the view region of GPI. The frequency response of this analysis of velocity $\leqslant$6 kHz, is set by the $\sim 164\,\mu$s duration of the coherent time interval. The time resolution of velocity is high enough to investigate the flow velocity changes during I-phase which we focus on in this paper.

Another reason for not choosing 2D time-delay cross-correlation analysis as the analysis method for GPI data is that the viewing region inside the separatrix of GPI in EAST is relatively small, so there is not sufficient space for a 2D time-delay cross-correlation analysis inside the separatrix. Like traditional TDE method, the dynamic based TDE also can't detect the velocity field in H-mode well, since there aren't enough eddies for calculation.

4. Application to GPI data during dithering L–H transition

Nowadays, an intermediate oscillatory state during the L–H transition with margin heating power injection, termed an I-phase, has been widely recognized by the fusion community. Studying the I-phase on EAST can make a strong contribution to ITER, which will have a very marginal power injection during its first run. Figure 4 shows a typical double null (DN) H-mode discharge (shot 41363) with a toroidal magnetic field $B_\phi \sim 1.8$ T in the counter-clockwise direction viewing from top. The plasma current $I \sim 400$ kA and the electron density $n_e \sim 2.8 \times 10^{-19}\,\mathrm{m^{-3}}$ are shown in figures 4(*a*) and (*b*), respectively. The auxiliary heating power levels of lower hybrid wave (LHW) and ion cyclotron resonance frequency (ICRF) are $\sim$1.2 MW and $\sim$1.1 MW respectively as shown in figure 4(*c*).

The red line in figure 4(*d*) is Dα emission detected at the lower divertor region by a filter-scope diagnostic. From 3.500 to 3.522 s is L-mode, but there are two dithering cycles in L-mode. From 3.522 to 3.530 s is the I-phase (dithering phase) and the plasma enters an ELMy-free H-mode at 3.530 s. The time in figures 4(*e*) and (*f*) corresponds to the time slice marked in the black box in figures 4(*a*)–(*d*). The time dependence of the poloidally averaged He I line emission from the GPI diagnostic just outside the separatrix at $r - r_{sep} = 0.9$ cm is shown by the black line in figure 4(*e*). The peak of the Dα signal lags about 180–200 μs behind the peak of the upper GPI signal, since the Dα emission (red line) is detected at the lower divertor region by filter-scope diagnostic. This delay is consistent with the timescale for parallel flow loss in the scrape-off layer (SOL): $\tau_\parallel = L_\parallel/(M_\parallel c_s)$ (where the viewing regions of the upper GPI and filter-scope are separated by $L_\parallel \sim 4$ m in total field direction, Mach number $M_\parallel \sim 0.4$, $T_i \approx T_e \sim 25$ eV, so the sound speed $c_s = (2T_e/m_i)^{1/2} \sim 50\,\mathrm{km\,s^{-1}}$, thus $\tau_\parallel \sim 200\,\mu$s) in EAST. The whole process of 3 typical dithering cycles are presented in figure 4(*f*), including three bursts in which the GPI intensity signal rapidly expands both radially inward and outward from separatrix respectively e.g. at 3.5225 s. For each of the three dithering cycles, there are always two or even more small bursts. That means, a dithering cycle burst always has fine structure which the filter-scope diagnostic (Dα line) does not distinguish this, possibly due to its much lower temporal resolution (100 kHz) than that of GPI on EAST.

Based on the temporal evolution of the normalized GPI signal displayed in figure 4(*e*), we define a complete dithering cycle as a period between two adjacent times at which the GPI signal begins to increase dramatically. The first part of a dithering cycle during which the GPI signal has a rapid increase is defined as the turbulent period, while the rest of a dithering cycle during which the GPI signal has a relatively slow decreasing trend is defined as the quiescent period. Take figure 4(*e*) for example, a typical dithering cycle is defined as the period between t1 and t3, and t2 should be the cut-off time between the turbulent and quiescent periods, at which the GPI signal reaches the maximum in amplitude. Combining figures 4(*e*) and (*f*), one should conclude that during the

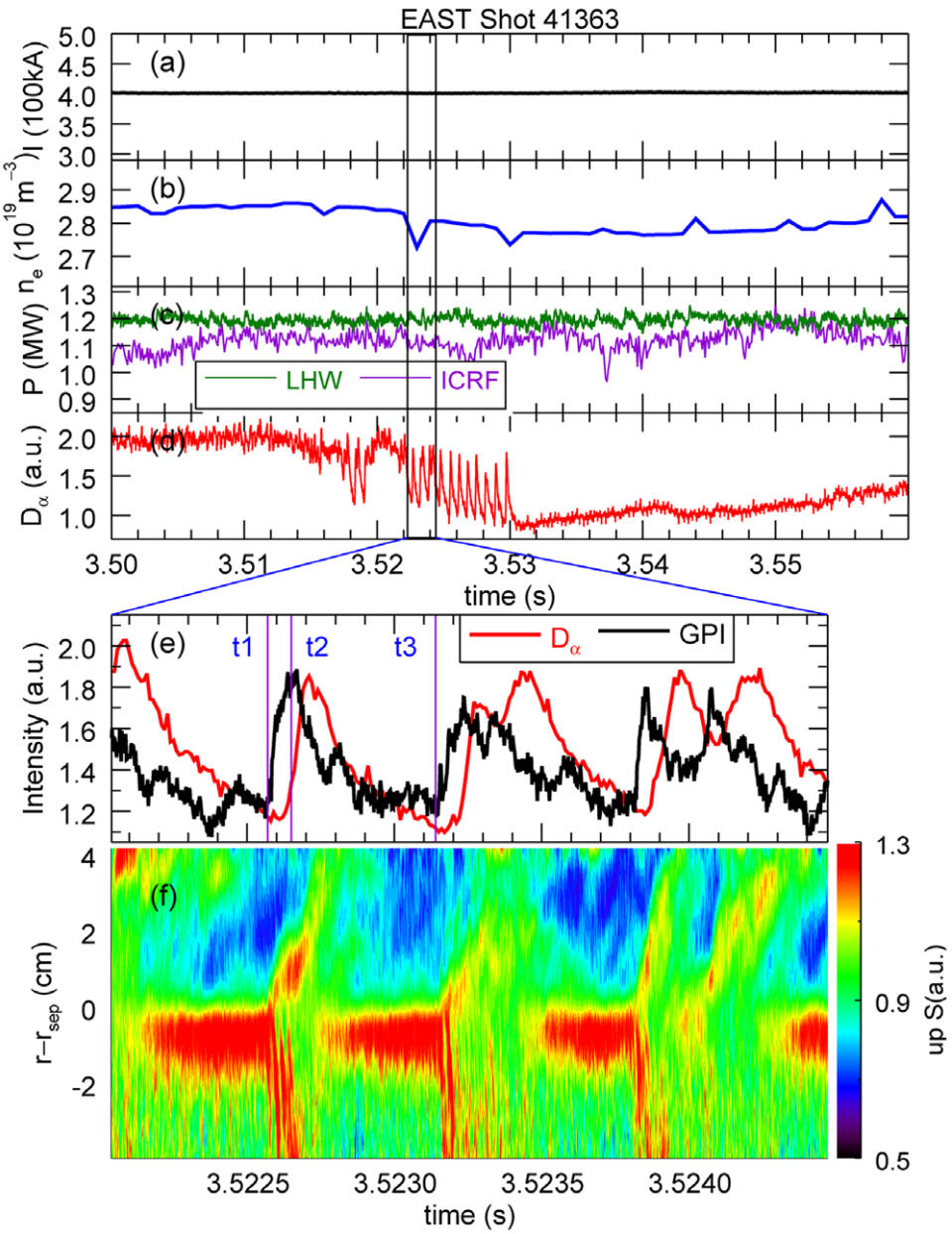

Figure 4. (*a*) Time dependence of (*a*) plasma current, (*b*) electron density, (*c*) power of LHW and ICRF, (*d*) Dα line. (*e*) Time dependence of normalized He I line emission from GPI diagnostic just outside the separatrix at $r - r_{sep} = 0.9$ cm (poloidal average) and the red line is Dα line detected at the lower divertor region. (*f*) Time dependence of poloidally averaged radial profile of GPI normalized images. The time slice of (*e*) and (*f*) is within the black box in (*a*), (*b*), (*c*) and (*d*) at the top.

quiescent period of every dithering cycle the GPI emission fluctuation grows with time just inside a narrow radial area $r - r_{sep} = -2 \sim 0$ cm, and at beginning of the turbulent period the GPI emission fluctuation seems to burst by propagating both inward and outward.

The process of dithering burst is surely of interest, but we are also interested in the evolution of turbulence during a dithering burst. Figure 5(*a*) shows a sequence of five normalized zero-time delay spatial cross-correlation images evaluated over a period of $\sim$180 μsec during a dithering cycle, where each image is correlated over 14 frames ($\sim$35 μsec). These images show the structure of turbulence during a dithering burst process in the upper GPI, and the time evolution of Dα line as detected from lower divertor region. Before calculating cross-correlation coefficient at zero-time lag between signals at two pixels, a band-pass filter of 20–60 kHz. The region in the limiter shadow, which is outside the range of interest (top right region of every graphic), is colored light green. Normally, the poloidal flow in EAST [28] is in the ion diamagnetic direction (IDD) in the SOL and in the electron diamagnetic direction (EDD) inside the separatrix. Figure 5(*b*) shows the poloidal velocity estimated by the dynamic programming based TDE technique on GPI data (using 141 frames), which has a poloidal turbulence flow in the EDD inside the separatrix and in the IDD outside the separatrix, i.e. consistent with previous results in EAST. In

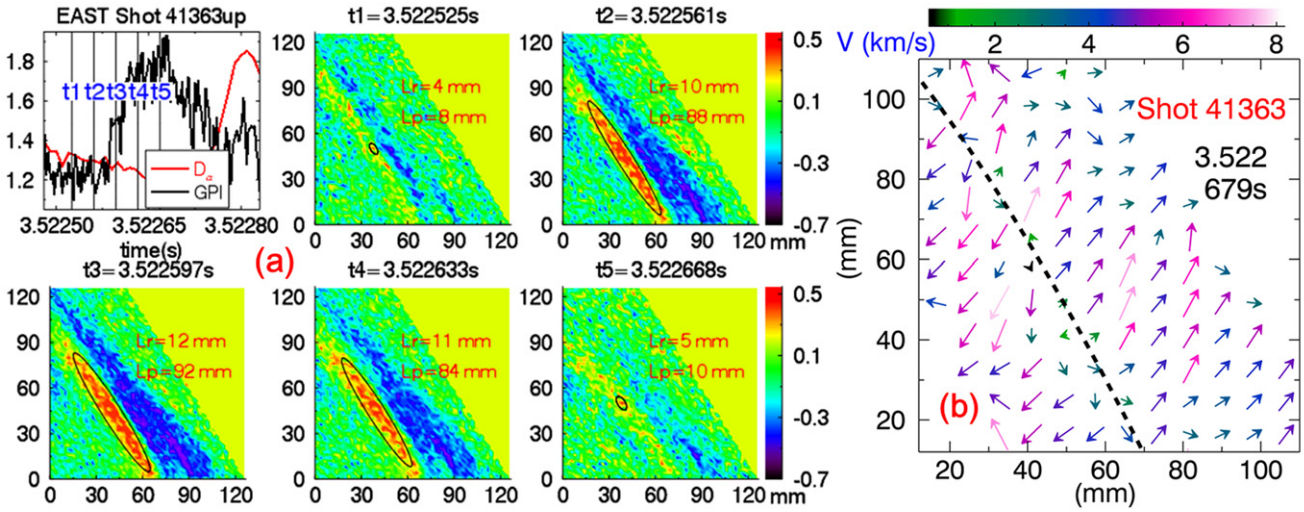

Figure 5. (*a*) Sequence of normalized zero-time delay cross-correlation images (reference pixel [19, 25] located inside the separatrix) during a typical dithering burst process. Time dependence of He I line emission is from GPI diagnostic within 4 pixels just outside the separatrix at $r - r_{sep} = 0.9$ cm and the Dα line is detected from the lower divertor region. The times t1–t5 in the cross-correlation images are labeled in the first image. (*b*) Velocity image calculated by dynamic programming based TDE at $t = 3.522\,679$ s. The lengths and colors and directions of the arrows indicate the magnitude and direction of the velocities. The black dash line is the poloidal velocity reversing boundary (flow moves inward and downward inside the dash line, while moves outward and upward outside the dash line).

figure 5(*b*) the black dashed line is the boundary separating the EDD flow from the IDD flow, which closely corresponds to the separatrix location from EFIT.

The cross-correlation lengths L_r and L_p representing the radial and poloidal structure scale of turbulence are shown in figure 5(*a*). The image at t3 (3.522 597 s) is regarded as the starting frame of the dithering burst. Images at t1–t3 in figure 5(*a*) show that L_r and L_p increase before the dithering burst from 4 mm width and 8 mm length at t1 to 12 mm width and 92 mm length at t3, and decrease after the burst as shown in images at t3–t5. The L_r and L_p change in the same way in every dithering cycles in shot 41363 and in shots 41362 and 41364, which have almost the same discharge parameters as shot 41363. This means that the turbulence structure scale increases before a dithering burst and decreases after burst.

As mentioned in the introduction in section 1, to better understand the edge turbulence and its relationship to edge transport during I-phase (dithering phase), the radial and poloidal flow pattern in the plasma edge should be determined. To achieve this, the dynamic programming based TDE method is applied to GPI video images here. Two dim gray vertical solid lines at ~3.522 and ~3.530 s in figure 6 are the dividing lines between L mode, I phase (i.e. dithering phase) and H mode. The quasi-periodic dithering bursts in the GPI in the I-phase are also seen in the Dα signal increasing and decaying in figure 6(*c*). It has been found that in I-phase, the radial fluctuation velocity V_r can be intermittently up to $\sim 2.0\,\mathrm{km\,s^{-1}}$ both outward and inward from the separatrix in the radial direction (see figure 6(*a*)), and the poloidal velocity V_p can up to $\sim 4.0\,\mathrm{km\,s^{-1}}$ in the ion diamagnetic drift direction in SOL and $\sim -3.0\,\mathrm{km\,s^{-1}}$ in the electron diamagnetic drift direction inside the separatrix (see figure 6(*b*)).

The radial profile of the poloidal flow shear $\partial V_p/\partial r$ around the separatrix and the auto-correlation time of temporal signals τ_{ac} inside and outside the separatrix within a band-pass filter (8–40 kHz), rise with dithering bursts as shown in figures 6(*c*) and (*d*), respectively. A secondary increase of the auto-correlation time is found after most dithering bursts as shown in the slender magenta box at ~3.5275 s in figures 6(*c*) and (*d*), possibly due to two small bursts during a big dithering burst. There are 2–3 dithering bursts from 3.517–3.519 s shown in the black ellipse in L-mode i.e. L–I–L transition, and all features, i.e. radial and poloidal velocities, poloidal flow shear and auto-correlation time, vary in the same way as the dithering cycles during L–I–H transition. Figures 6(*a*) and (*b*) show that small bursts still happen intermittently after the H-mode is established.

For a better understanding of the dynamics of turbulence during dithering cycles, a more detailed analysis is needed. A comparison between two signals from the upper and lower GPI is shown in figure 7 to see whether the dithering bursts are occurring in the same phase. The time dependence of normalized signals S1 and S2 in figures 7(*a*) and (*b*) are from two pixel signals of the upper GPI images at $r - r_{sep} = -0.4$ cm with 52° and 48° poloidal angles, respectively. Signal S3 in figure 7(*c*) comes from a pixel of the lower GPI, which is separated by 66.6° toroidally from S1 and S2, and is vertically symmetric about the midplane with S2. These signals increase and decrease quasi-periodically and signals S2 and S3 are almost in phase. From the fast magnetic probes on EAST, the toroidal mode number of the dithering is estimated to be 0. Thus, the GPI fluctuation measurements during dithering bursts is compatible with a $m = 0$ mode.

Normalized signal S4 and its enveloped Hilbert transform [29] within a band-pass filter from 8 to 40 kHz as shown in figures 7(*d*) and (*e*) is calculated from a pixel of the upper GPI images at $r - r_{sep} = 0.8$ cm and 51° in the poloidal direction. In mathematics and signal processing, the Hilbert transform is a linear operator which takes a function, $u(t)$, and produces a

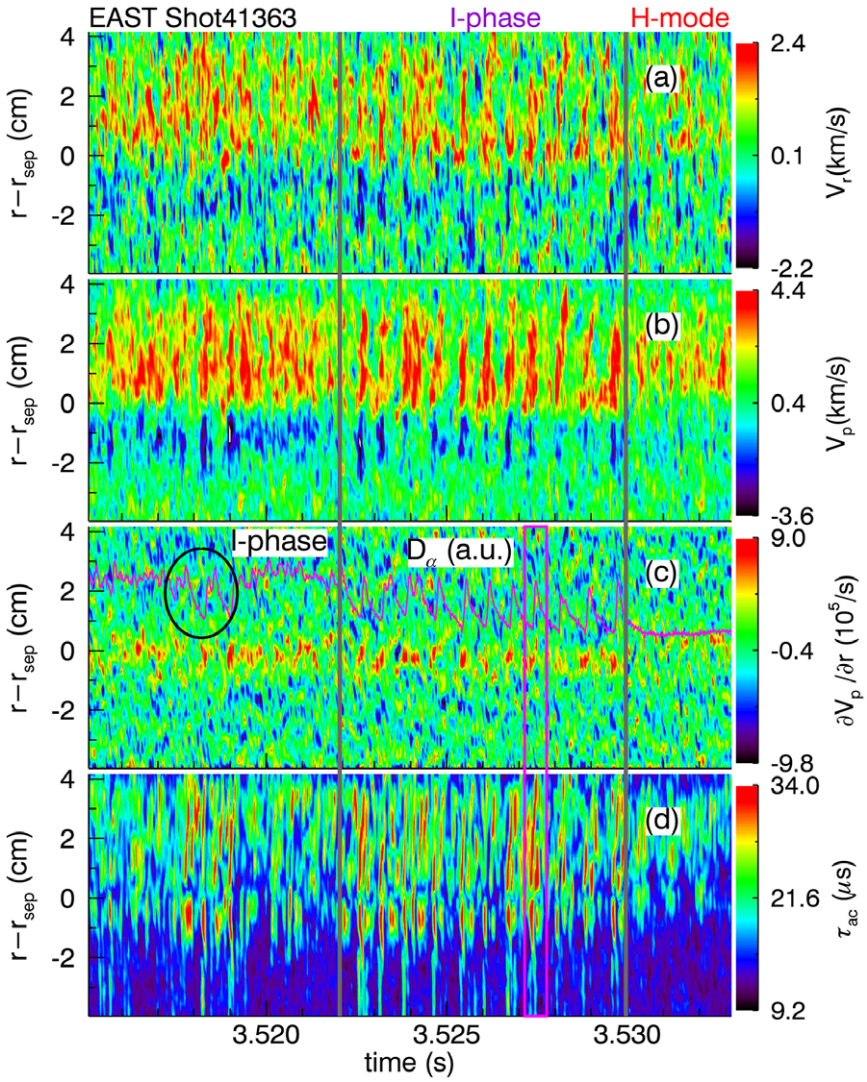

Figure 6. Time dependence of poloidally averaged radial profile of (*a*) radial velocity, (*b*) poloidal flow velocity, (*c*) poloidal flow velocity shear and (*d*) auto-correlation time from Shot 41363. Dα line (the dark violet line) in (*c*) is measured in lower divertor region by filter-scope.

function, $H(u)(t)$, as:

$$H(u)(t) = \frac{1}{\pi}\text{p.v.}\int_{-\infty}^{\infty}\frac{u(t)}{t-\tau}\mathrm{d}\tau, \tag{10}$$

where p.v. is the Cauchy principal value of the integral. It is a basic tool in Fourier analysis, and provides a concrete means for realizing the harmonic conjugate of a given function or Fourier series. Here we utilize the Hilbert transform to calculate the amplitude of turbulence fluctuation. The time at maximum of the envelope of signal S4 is consistent to the beginning of a dithering burst here. Similar to the process of sawtooth crash on $q = 1$ flux surface, the turbulence gains energy gradually before bursting, and then bursts dramatically when over a certain magnitude (the intensity of normalized signals is proportional to local turbulence fluctuation). The dithering burst occurs when the auto-correlation time of local flow fluctuation τ_{ac} inside the separatrix reaches its maximum $\sim$30 μs (see figures 7(*e*)–(*g*)). Like the evolution of cross-correlation length in figure 5(*a*), the radial and poloidal flow velocity in figure 7(*i*) and auto-correlation time (see figures 7(*e*)–(*g*)) inside of separatrix rise before a dithering burst and decrease after the burst. In most cases, the poloidal flow shear rises before a dithering burst and decreases after the dithering burst around the separatrix, but it is hard to find a consistent evolution of poloidal flow shear inside of separatrix. This case is shown in figures 6(*c*) and 7(*j*).

To further ascertain the temporal evolution of poloidal velocity V_p, as well as that of radial shear of poloidal velocity $\partial V_p/\partial r$, which has been displayed in figures 7(*i*) and (*j*) in a small period of time with only approximately three dithering cycles, figure 8 shows the evolution of these two quantities during the turbulent periods or the quiescent periods. Figures 8(*a*)–(*c*) exhibit the estimates of V_p in three consecutive discharges, i.e., shot 41362–41364, while related results for $\partial V_p/\partial r$ are shown in figures 8(*d*)–(*f*). From these figures, the estimated quantities of V_p or $\partial V_p/\partial r$ during the two periods show consistent results among these three shots. Specifically, in turbulent period, the time-averaged poloidal velocity just inside the seperatrix is in EDD. But in quiescent period, the time-averaged poloidal velocity seems not to be in EDD inside the separatrix but rather in the IDD, and the

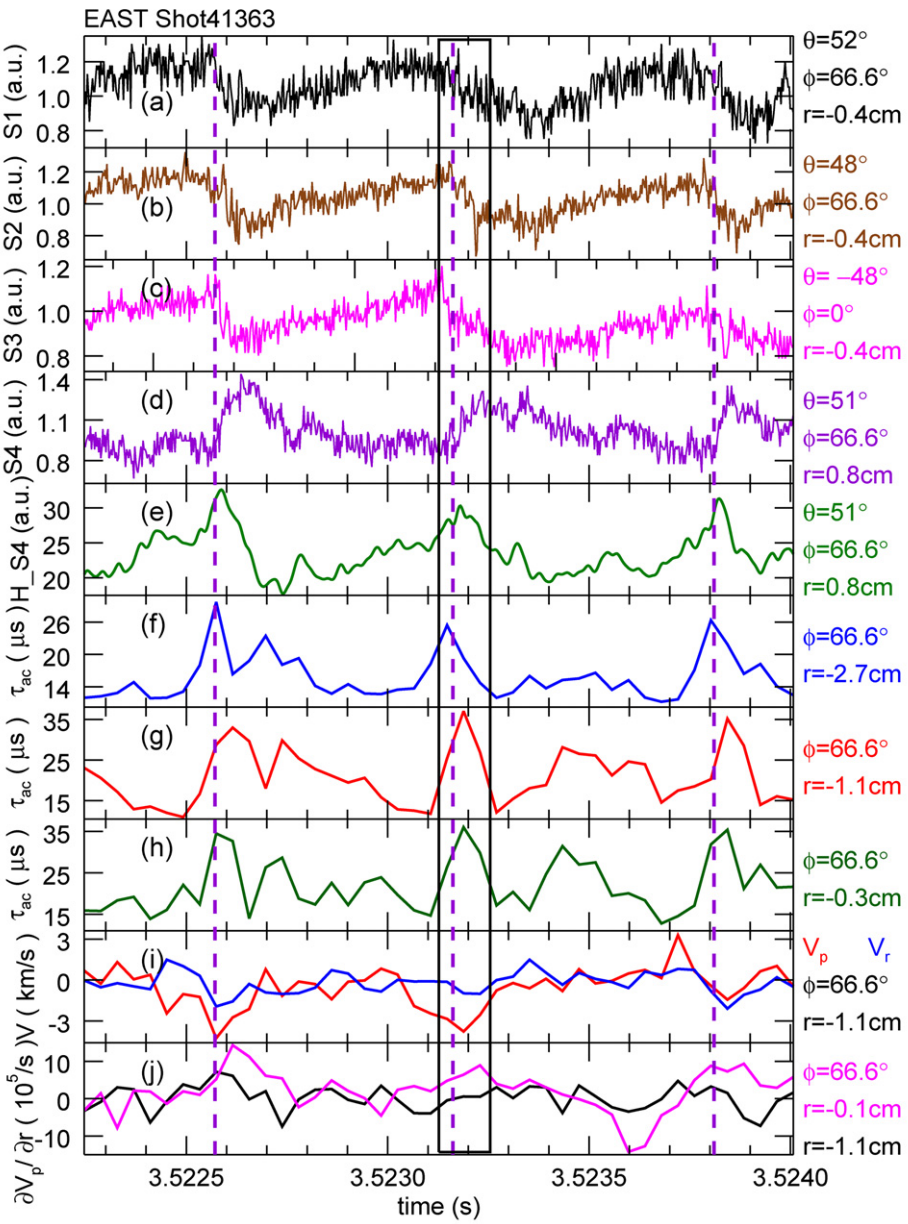

Figure 7. Time evolution of GPI He I normalized signals S1 (*a*), S2 (*b*), S3 (*c*) from three pixels at different position but same radial location ($r - r_{sep} = -0.4$ cm) during the dithering phase for shot 41363. S3 comes from the lower GPI, separated about 66.6° toroidally from S2 and S3, and vertically symmetrical about the midplane with S2. (*d*) Normalized signal S4 from a pixel of up GPI images outside the separatrix at $r - r_{sep} = 0.8$ cm. (*e*) Hilbert transform of S4 filtered by a band-pass filter from 8 to 40 kHz. Time dependence of the auto-correlation time of edge plasma fluctuation filtered by a band-pass filter from 8 to 40 kHz in I-phase at $r - r_{sep} = -2.7$ cm (*f*), -1.1 cm (*g*) and -0.3 cm (*h*) from up GPI. (*i*) Time dependence of poloidal (red line) and radial (blue line) velocities at $r - r_{sep} = -1.1$ cm from the upper GPI. (*j*) Time dependence of poloidal flow shear at $r - r_{sep} = -0.1$ and -1.1 cm from the upper GPI. The three dark violet vertical dash lines indicate the start time of dithering bursts. The time interval in the black rectangle represents the turbulent period of a typical dithering cycle.

poloidal flow velocity outside the separatrix is less than that in turbulent period as shown in figures 8(*a*)–(*c*). These results are similar to the E_r profiles during turbulent and quiescent period measured by Doppler reflectometry in ASDEX-U [30]. The poloidal flow shear around the separatrix in the turbulent period is much larger than that during the quiescent period, but not at other radial positions in figures 8(*d*)–(*f*). That is because the poloidal velocity in the EDD decreases just inside the separatrix while increasing dramatically outside the separatrix, and the poloidal flow shear in turbulent period around the separatrix is much larger than that at the quiescent period.

The time-averaged poloidal velocity just inside the separatrix is in the EDD in the turbulent period, while it seems to be in IDD in the quiescent period as shown in figures 8(*a*)–(*c*). That is possibly because the plasma collisionality decreases [31, 32]; a decrease in the electron density and increase in the electron temperature have been measured by reciprocating probe from turbulent period to quiescent period in dithering cycles in EAST as shown in

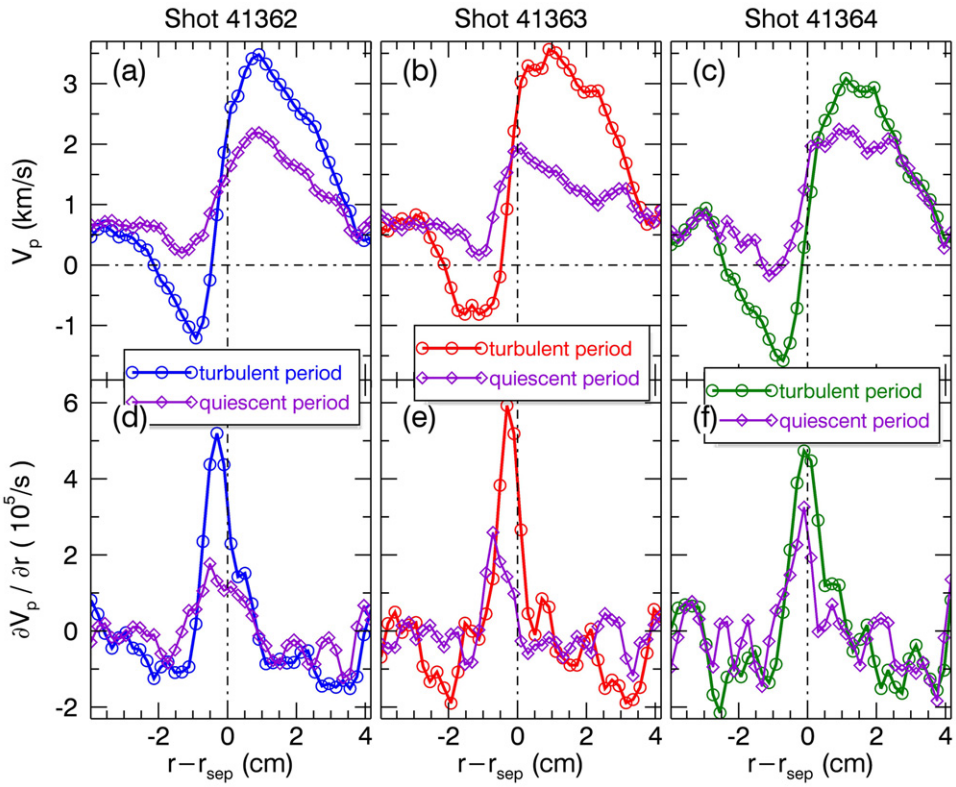

Figure 8. The profile of the averaged poloidal velocity during all turbulent and quiescent periods of (*a*) shot 41362, (*b*) shot 41363 and (*c*) shot 41364. The profile of the averaged ploloidal flow shear during all turbulent and quiescent periods at (*a*) shot 41362, (*b*) shot 41363 and (*c*) shot 41364.

figures 9(*c*) and (*d*). Figure 9(*a*) is the Dα line from L-mode to I-phase measured by filter-scope at the lower divertor region. The poloidal velocity evaluated by dynamic programming based on TDE and the polodial $E \times B$ drift velocity are shown in figure 9(*b*). The polodial $E \times B$ drift velocity is in EDD in L-mode, while reverses to IDD when entering I-phase and sharply decreases into EDD after that, which is shown in figure 9(*b*). As the result from GPI, the poloidal velocity calculated by dynamic programming based on TDE from probe reverses intermittently from $\sim -10\,\mathrm{km\,s^{-1}}$ (EDD) to $\sim 10\,\mathrm{km\,s^{-1}}$ (IDD) inside the separatrix at $r - r_{\mathrm{sep}} = -0.5\,\mathrm{cm}$ during I-phase. But the poloidal velocity does not always reverse after a dithering burst as shown in figures 6(*b*) and 7(*i*). That is possibly because the different discharging condition, where the Dα signal decreases much more sharply in shot 42160 than that in shot 41363 after the plasma entering I-phase.

In figure 9(*b*), the poloidal velocity inferred from the dynamic programming based on TDE analysis of the Langmuir probe data is compared with the poloidal velocity inferred from Langmuir probe potential profiles. However, the time behavior of the two velocities is different. To better understand this, the radial force balance equation is needed as shown below:

$$E_r = \frac{1}{Z_i e n_i}\frac{\partial p}{\partial r} - \vec{e}_r \cdot (\vec{v}_i \times \vec{B}). \tag{11}$$

From equation (11), we can infer that the polodial $E \times B$ drift velocity mainly responses both poloidal velocity and radial pressure gradient. Although the poloidal velocity reverses intermittently inside the separatrix, the radial edge plasma pressure gradient increases during I-phase. Thus, the polodial $E \times B$ drift velocity rises gradually in EDD, which behaves differently from that of poloidal velocity during I-phase.

5. Summary

Dual gas puff imaging diagnostic systems have been installed on the EAST tokamak and have provided 2D imaging of edge plasma turbulence during L-mode, ELMy H-mode and ELMy-free H-mode during the recent experimental campaign. Utilizing the dynamic programming based TDE analysis, poloidal and radial time-resolved local flow velocities during a dithering L–H transition have been obtained, revealing many interesting details about the dynamic process of dithering bursts.

Local poloidal flow velocities up to $\sim -3\,\mathrm{km\,s^{-1}}$ (in EDD) and radial flow velocities up to $\sim -2\,\mathrm{km\,s^{-1}}$ (inward) are found inside the separatrix during dithering turbulent periods. The mode number of dithering cycles appears to be (0,0), and a big dithering burst consists of two or even more small bursts. The poloidal flow shear just around the separatrix in turbulent period is much larger than that at quiescent period, and larger than that found at other radial positions.

To decrease the volume of the gas puff, a new supersonic GPI injector will be employed in the next EAST campaign to improve the spatial resolution of the dual GPI system. A higher efficiency optical system is also under design to improve the

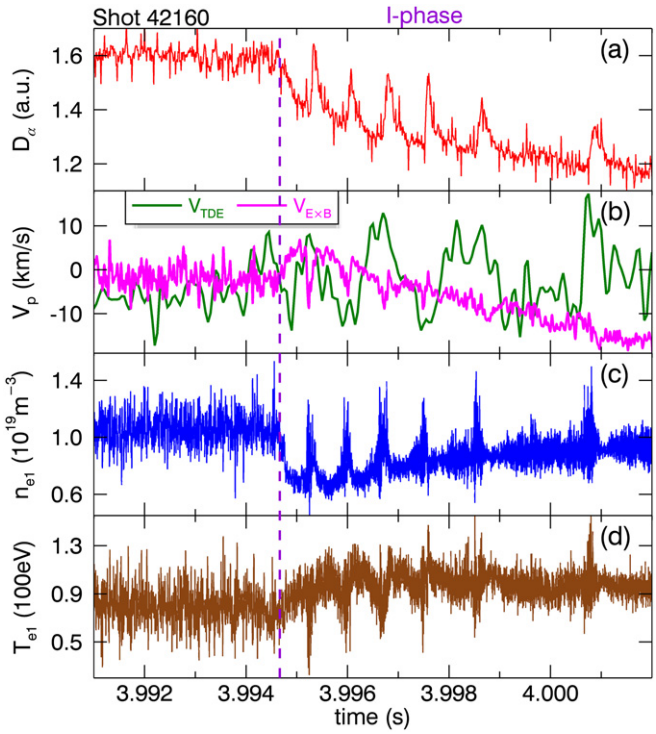

Figure 9. Time evolution of (*a*) Dα signal detected in lower divertor region, (*b*) poloidal velocity calculated by dynamic programming based on TDE and $E_r \times B$ drift velocity, (*c*) electron density inside the separatrix at $r - r_{sep} = -0.5$ cm, (*d*) electron temperature inside the separatrix at $r - r_{sep} = -0.5$ cm.

signal-noise ratio of GPI in the next campaign, when the GPI will play an important role in edge plasma research.

Acknowledgments

The authors gratefully acknowledge the contribution of the EAST staff and the fruitful discussions with Y Chen, H Y Wang and S B Xia. This work was supported by the National Magnetic Confinement Fusion Science Program of China under Contracts No 2011GB107001, No 2011GB107003, No 2012GB101000 and No 2010GB104001, No 2013GB107003 the National Natural Science Foundation of China under Contracts No 11205193, No 11075181, No 11021565, No 10990212, No 11105177 and the Sino Danish Center for Education and Research.

References

[1] Burrell K H 1997 *Phys. Plasmas* **4** 1499
[2] Antoni V *et al* 2003 *J. Nucl. Mater.* **313–316** 972–5
[3] Wagner F 2007 *Plasma Phys. Control. Fusion* **49** B1–33
[4] McKee G, Ashley R, Durst R, Fonck R, Jakubowshi M, Tritz K, Burrell K, Greenfield C and Robinson J 1999 *Rev. Sci. Instrum.* **70** 913
[5] Heidbrink W W, McKee G R, Smith D R and Bortolon A 2011 *Plasma Phys. Control. Fusion* **53** 085007
[6] Tobias B *et al* 2010 *Rev. Sci. Instrum* **81** 10D928
[7] Yun G S *et al* 2010 *Rev. Sci. Instrum* **81** 10D930
[8] Mazzucato E 2001 *Nucl. Fusion* **41** 203
[9] Munsat T 2003 *Rev. Sci. Instrum.* **74** 1426
[10] Maqueda R J 2003 *Rev. Sci. Instrum.* **74** 2020
[11] Liu S C 2012 *Rev. Sci. Instrum.* **83** 123506
[12] Zweben S J 2006 *Phys. Plasmas* **13** 056114
[13] Myra J R, D'lppolito D A, Stotler D P, Zweben S J, LeBlanc B P, Menard J E, Maqueda R J and Boedo J 2006 *Phys. Plasmas* **13** 092509
[14] Zweben S J *et al* 2012 *Plasma Phys. Control. Fusion* **54** 025008
[15] Zweben S J *et al* 2010 *Phys. Plasmas* **17** 102502
[16] Maqueda R J, Maingi R and the NSTX Team 2009 *Phys. Plasmas* **16** 056117
[17] Sechrest Y, Munsat T, Battaglia D J and Zweben S J 2012 *Nucl. Fusion* **52** 123009
[18] McKee G R Fonck R J, Gupta D K, Schlossberg D J, Shafer M W, Holland C and Tynan G 2004 *Rev. Sci. Instrum.* **75** 3490–2
[19] Holland C, Tynan G R, McKee G R and Fonck R J 2004 *Rev. Sci. Instrum.* **75** 4278–80
[20] Jakubowski M, Fonck R J, Fenzi C and McKee G R 2001 *Rev. Sci. Instrum.* **72** 996
[21] Gupta D K, McKee G R and Fonck R J 2010 *Rev. Sci. Instrum.* **81** 013501
[22] Schlossberg D J, Gupta D K, Fonck R J, McKee G R and Shafer M W 2006 *Rev. Sci. Instrum.* **77** 10F518
[23] Quénot G M, Pakleza J and Kowalewski T A 1998 *Exp. Fluids* **25** 177
[24] Wan B N *et al* 2009 *Nucl. Fusion* **49** 104011
[25] Munsat T and Zweben S J 2006 *Rev. Sci. Instrum.* **77** 103501
[26] Maqueda R J *et al* 2003 *Rev. Sci. Instrum.* **74** 3
[27] Fedorczak N, Manz P, Thakur S C, Xu M, Tynan G R, Xu G S and Liu S C 2012 *Phys. Plasmas* **19** 122302
[28] Xu G S *et al* 2011 *Plasma Sci. Technol.* **13** 397
[29] Jha R, Raju D and Sen A 2006 *Phys. Plasmas* **13** 082507
[30] Conway G D, Angioni C, Ryter F, Sauter P, Vicente J and the ASDEX Upgrade Team 2011 *Phys. Rev. Lett.* **106** 065001
[31] Ida K *et al* 2005 *Nucl. Fusion* **45** 391–8
[32] Yoshinuma M, Ida K, Yokoyama M, Nagaoka K, Osakabe M and the LHD Experimental Group 2009 *Nucl. Fusion* **49** 075036